CONFERENCE PRE-PRINT

TUNGSTEN EUV AND SOFT-X RAY EMISSION MEASUREMENTS, MODELLING AND ARTIFICIAL INTELLIGENCE ANALYSIS AT THE WEST TOKAMAK

R. GUIRLET CEA, IRFM, Saint-Paul-lez-Durance, France Email: remy.guirlet@cea.fr

P. MANAS CEA, IRFM, Saint-Paul-lez-Durance, France

C. DESGRANGES CEA, IRFM, Saint-Paul-lez-Durance, France

O. PEYRUSSE Aix-Marseille Université-CNRS, LP3 Marseille, France

N. SAURA ITER Organization

T. BARBUI Princeton Plasma Physics Laboratory Princeton NJ, USA

S. MAZZI CEA, IRFM, Saint-Paul-lez-Durance, France

The WEST team http://west.cea.fr/WESTteam

Abstract

Tungsten radiation in the WEST tokamak is diagnosed with several diagnostics. The main tool discussed in this article is an extreme-ultraviolet (EUV) spectrometer. Two examples of analysis are reported. The first one is the W density determination from measurements of well identified spectral lines of W⁴²⁺ to W⁴⁴⁺ in X-point radiation regime. The W density is found to be similar to values in a standard attached scenario, in agreement with a synthetic bolometry diagnostic. The second example concerns the 45-65 Å quasicontinuum emitted by a group of W ionisation stages. First, a Principal Component Analysis (PCA) allows to evidence the correlation between the spectral shape and the maximum electron temperature along the line of sight of the spectrometer. Then, the measurements are analysed with a Random forest algorithm which shows that the temperature can be predicted from a single spectrum within an uncertainty better than 100 eV. Finally, a semi-statistical structure and collisional-radiative model is applied to model the W ionisation balance. The result is closer to experimental values than models using a detailed energy level description. The modelled spectrum in the EUV and soft-X ray range shows good similarity with the WEST measurements. Further work will include an AI-aided tomographic inversion of the quasicontinuum measurements and a detailed study of the modelled temperature dependence of this quasicontinuum.

1. INTRODUCTION

With the choice of Tungsten as the main wall material of ITER and the subsequent equipment of several major devices (e.g. ASDEX-Upgrade [1], JET [2], WEST [3]) with solid Tungsten or Tungsten-coated plasma-facing components, radiative losses and fuel dilution set limitations to the operational domain of fusion devices. It is hence essential to diagnose W transport and density in those devices.

Contrary to other diagnostics (bolometry and most of soft-X ray diagnostics), which are sensitive to all impurities and cannot distinguish between them without assumptions and modelling. Extreme UV (EUV) spectroscopy offers

the advantage of providing species-resolved information. The spectra of light and mid-Z impurities are relatively simple (the number of emitted spectral lines in any given wavelength interval is relatively small) and the atomic data necessary to interpret them are relatively well known. Conversely, the extremely complex spectral structure of W emission makes the measurement analysis complex and time consuming. Nevertheless, it can provide a wealth of information about the plasma behaviour and is thus worth substantial experimental and modelling efforts such as those reported here.

In this article, we discuss three aspects of our W spectroscopic analysis focussed on the EUV spectrometer operated on WEST: *i*) W density determination in the plasma core of routinely performed LH-heated plasmas, *ii*) modelling of a prominent W feature emitted at 45-65 Å by means of a method adapted from high-density (laser-produced) plasmas, *iii*) electron temperature determination from an artificial intelligence (AI) analysis. Those examples show that EUV spectroscopy measurements bring an essential contribution to the physics of many-electrons systems. From a more practical point of view, it is a unique technique for a detailed analysis of W transport and radiation in fusion devices. It is also well suited to more global consistency studies of plasma measurements.

2. DIAGNOSTIC SET-UP

WEST is equipped with two extreme-ultraviolet (EUV) grazing incidence spectrometers [4]. The one on

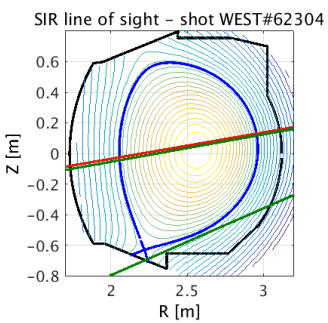


Figure 1: WEST magnetic equilibrium for discharges WEST#62034. Red line: typical fixed line of sight, green lines: extreme lines of sight in oscillating mode.

which the present study is based can scan the range 15-340 Å with two detectors mobile along the Rowland circle. During an experimental day, the detector position can be adjusted before each plasma discharge. The wavelength interval covered by a single detector is about 25 Å at the short wavelength end of the domain and about 60 Å at the long wavelength end. The acquisition time is 15 ms. The spectrometer has a single line of sight which can be rotated around a horizontal axis so that it sweeps periodically the lower half of the plasma from slightly above the magnetic axis down to the divertor region and further out, as shown by the green lines in Fig. 1. The minimum sweeping period is 4 s and it can be extended if the plasma is stationary for long enough and if a particularly fine spatial sampling is required (the longest period we have used up to now is 30 s). When the spectrometer is fixed, the line of sight is usually nearly horizontal and views slightly above the magnetic axis (see Fig. 1, red line). Two wavelength intervals are of particular interest for the present study:

1) the position 115-165 Å comprises spectral lines emitted by W^{42+} to W^{45+} from which the W density can be derived, as already shown in [5]. At the time of that publication, we did not have the data from other

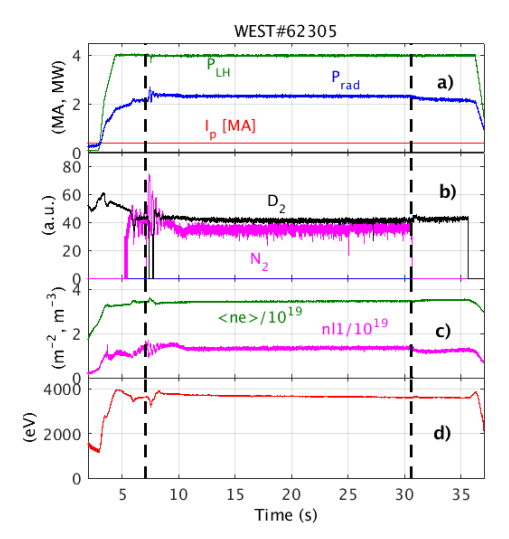
diagnostics such as bolometry and soft-X ray and thus were not able to compare our results with independent evaluations of the W density. Here we compare our EUV evaluation with that provided by an independent method based on bolometry measurements for the particular X-point radiation scenario;

2) the position 40-70 Å allows to observe a W quasicontinuum feature at 45-65 Å already reported in many fusion devices (see e.g. [1, 6]) and often used for W density evaluations; in this study we report on an AI analysis which aims at relating the observations with the electron temperature as measured by the electron cyclotron emission (ECE) radiometer. It has 32 measurement points distributed in the horizontal plane on both sides of the magnetic axis. The discharges analysed here were all heated by the Lower Hybrid (LH) wave at a power level of 4 MW. As a consequence, the measurements beyond a normalised radius of about $\rho = 0.5$ were polluted by the frequency downshift due to the suprathermal electrons and have been discarded from our study.

3. W DENSITY PROFILES IN X-POINT RADIATION SCENARIO

The X-point radiation (XPR) regime has been observed in many tokamaks (e.g. inAlcator C-mod [7], JT-60 [8] ASDEX-Upgrade [9]). It is characterised by a highly radiating, localised region of the plasma just above the X-point. By means of a controlled nitrogen gas injection, it has been demonstrated in dedicated WEST experiments that it can be stabilised for several tens of seconds, with the advantage of reducing the heat and particle flux on the divertor plate with respect to the standard 'attached plasma' scenario. It has also been shown that, in the XPR regime, the energy confinement time is higher than in standard L-mode plasmas. An example of a XPR discharge is shown in Fig. 2. The transition occurs around 7.1 s as shown by the increase of the signal on the interferometry chord which views through the highly radiating region (in the particular case discussed here, an impurity burst occurred almost at the same time). After a transient phase of increase then decrease of the electron density and temperature, the plasma stabilises itself at a central temperature of about 3.7 keV for about 30 s. Two successive

and almost identical discharges are used here. In the first one (WEST#62304) the EUV spectrometer was in fixed mode with the line of sight slightly above the magnetic axis as shown in Fig. 1. In the second discharge (WEST#62305) the line of sight was oscillating at a period of 4 s between the extreme positions.



Global parameters of discharge Figure 2: WEST#62305. a) red: plasma current, green: LH power, blue: radiated power; b) black: D2 flow, magenta: N2 flow; c) green: volume average density, magenta: integrated density as measured by a chord through the XPR region; d) central electron temperature.

The observation of well resolved spectral lines emitted by W⁴²⁺ to W⁴⁵⁺ in the range 120-140 Å has already been reported elsewhere [5]. There is one spectral line for each of those ionisation stages. They are well resolved and their intensity is high enough to be measured if the electron temperature is above 2.8 keV over a substantial part of the line of sight. Given that WEST LH-heated plasmas have usually a central electron temperature of 3-4 keV (3.7 keV for the discharges analysed here), those spectral lines allow to access the core plasma dynamics. To determine more accurately the position at which the W density can be determined from the spectral line measurements, we have used the expression of a spectral line emissivity $\varepsilon_{Z,z}^{ij}$ as a function of the plasma quantities: $\varepsilon_{Z,z}^{ij} = n_e n_Z f_{Z,z} PEC_{Z,z}^{ij}$ where n_e and n_Z are the electron and emitting impurity

$$\varepsilon_{Z,Z}^{ij} = n_e n_Z f_{Z,Z} PEC_{Z,Z}^{ij}$$

densities, $f_{Z,z}$ is the fractional abundance of the emitting ionisation stage and $PEC_{Z,z}^{ij}$ the photon emission coefficient of the spectral line.

This expression was used to build a 1D (radial) emission model of the relevant lines in the plasma. The background plasma is described by the two-dimensional magnetic equilibrium calculated by the NICE code [10] and the electron density and temperature measurements from the interferometry and ECE diagnostics respectively. The W

ionisation balance is calculated using the data published for example in [11] and the photon emission coefficients (PEC) of the observed lines result from intermediate coupling calculations performed in the frame of the ADAS collaboration [12].

The results of such calculations are shown in Fig. 3 for discharge WEST#62304. It can be seen that prior to the XPR transition (around 6 s), the emission region of W⁴²⁺ is centred at $\rho = 0.1$, the more ionised stages emitting even closer to or at the magnetic axis. Α noticeable effect of the transition to XPR is that central electron temperature increases from around 3 to 3.6 keV so that the emission region of each W ion shifts away from the magnetic axis.

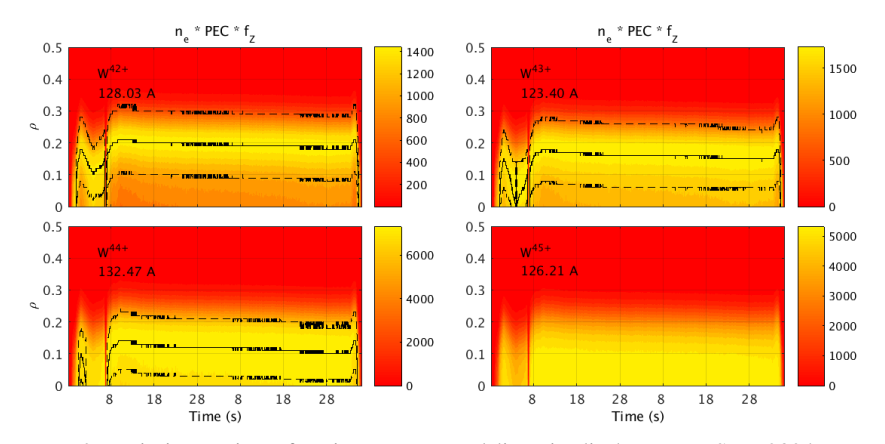


Figure 3: Emission region of various W spectral lines in discharge WEST#62304 as a function of time and radial coordinate.

Solid lines: position of maximum emission. Dashed lines encompass 70% of emission.

With the assumption of a weak W density gradient in the emission region of each spectral line and by combining the information from W^{42+} to W^{45+} , a W density profile is obtained close to the magnetic axis. With a 15 ms time resolution and a fixed, central line of sight, it is possible for example to evidence W accumulation in an ICRHheated plasma [5]. The results for the XPR discharge are shown in Fig. 4. The very peaked profile before transition is somewhat puzzling since in this type of discharge, turbulent transport is usually found dominant over neoclassical transport and thus rather flat impurity density profiles are expected. Nevertheless, the corresponding

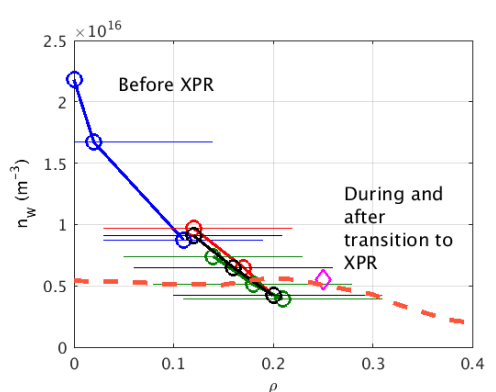


Figure 4: W density profile before (O), during (O) and after (O, O) transition to the XPR regime. Dashed line: W density from synthetic diagnostic. Horizontal bars represent the radial width of the 70% emission zone.

concentration (about 3×10^{-4}) is consistent with semiquantitative evaluations from other diagnostics along the experimental campaign

While we consider the time evolution of the EUV results as reliable, the fact that the absolute calibration was not done in many years leads us to question the accuracy of the absolute W density deduced from the EUV measurements. Another limitation is the rather narrow temperature (and thus radial) range in which the W density can be determined. An independent method has been developed to extract the W density from the (spectrally unresolved) bolometry diagnostic. A model of the plasma and of the diagnostic was built with the impurity density profiles as parameters. The various impurity (W and generic mid-Z and low-Z impurities represented by Cu and N resp.) densities are adjusted until the measurements on many lines of sight are satisfactorily reproduced (Cu and N are assumed homothetic to the electron density; below 1 keV, we make the assumption that the W density profile has the same shape as the

electron density). The results are shown on **Fig. 4** (dashed line) for the same discharge. Outside $\rho = 0.4$ (not shown on the figure), the W profile is not monotonic, a feature which is thought to arise from uncertainties in the bolometer inversion due to the limited number of active channels. The comparison of the two methods shows a relatively good quantitative agreement which gives us confidence in both methods and in the EUV spectrometer calibration.

Beside the main diode-based SXR array, WEST is also equipped with a multi-energy SXR camera (ME-SXR) [13]. It was not operational during the same discharges as the EUV spectrometer so the consistence check can be

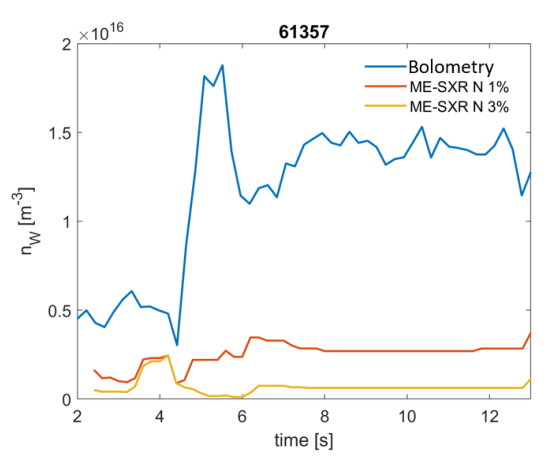


Figure 5: time evolution of the central W density determined the synthetic bolometry diagnostic (in blue) and from the ME-SXR measurement tomography assuming a N concentration of 1% (red) and 3% (orange).

done only with the synthetic bolometry diagnostic. Light impurities are the dominant contributors to the signal of the high-energy (5-6 keV) channels of that camera so those channels are used to infer the light impurity density. Their contribution (line and continuum radiation) is then subtracted from the signals of the low-energy (2-3 keV) channels so that the tungsten density can be deduced from the remaining signal, mostly made of W line emission. In practice, the W density is estimated by modeling the inverted radial emissivity profiles with an analytic tomography code based on plasma emissivity calculated with the FLYCHK spectral tool [14]. This method is described in detail in [15].

The comparison of the ME-SXR with the bolometry results are shown for discharge WEST#61357 in **Figure 5**. Due to the uncertainties, two assumptions were made about the light impurity density (represented again by a 'generic' N), namely 1% and 3%. It can be seen on the figure that indeed the resulting W density is very sensitive to this parameter. Nevertheless, it is also obvious that the ME-SXR-based method results are not

consistent with that based on bolometry. Even with the lower N concentration assumption, there is still a factor of about 4 between the two. Some of the discrepancy may be related to errors inherent to tomographic inversions and to the cooling functions calculated with FLYCHK. This code is known to be easy of use for general purposes but at the expense of a limited accuracy. In the near future, the model presented in the next section will be used to calculate the cooling function with a more complete description of the atomic structure.

4. COLLISIONAL-RADIATIVE MODELLING OF TUNGSTEN

The analysis presented above relies heavily on the knowledge of the W ionisation balance for the measurement localisation and on that of the photon emission coefficient for the density values. Both types of information are calculated by atomic structure collisional-radiative models. The ionisation balance used in the previous section comes from ADAS datasets adjusted on experimental results obtained in 2008 in ASDEX-Upgrade [10]. To our knowledge there has been no experimental check of those results since then. Moreover, other models differ by several units in the calculated average charge as a function of the electron temperature, as can be seen in Fig. 6. This is possibly due to the limited number of transitions included in the model and the difficulty to demonstrate

its completeness. We have used a configuration average (CA) model which, by considering global transitions between configurations, provides systematic calculations of global, ion and spectral parameters [16]. Conversely to a common approach which involves an independent calculation of the ionization equilibrium performed by means of global ionization and recombination rates followed by the excited state population calculation, our model allows to obtain the total set of configuration populations in a single step. For a given temperature, the configurations considered in the model belong to different charge states. The set of rate equations is expressed in standard compact matrix form dN/dt = T.Nwhere T is the configuration-average (CA) rate matrix and N is the population vector whose length corresponds to the list of the configurations supposed to be significantly populated.

A specificity of a high-Z complex element such as W is that above the first ionization threshold, there exist many multiply excited states that form resonances for the so-called resonant capture of free electrons (also called

Figure 6: Average charge of W ions as a function of the electron temperature. Examples of previously published data and our new calculations (ne = 5×10^{19} m⁻³) with various completeness levels (see text).

dielectronic capture, see for instance [17]). These states are likely to strongly affect the ionization balance. To select the most significant ones, we adopt a specific promotional strategy. At the lowest level of completeness

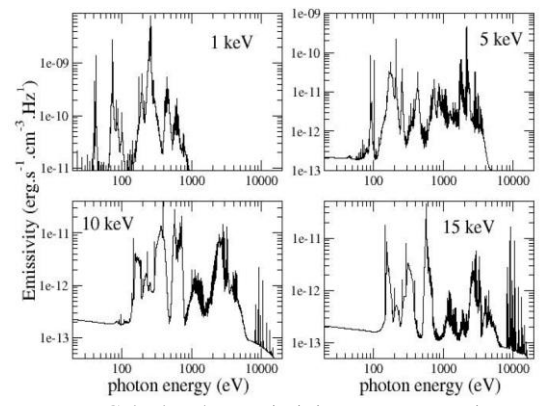


Figure 7: Calculated W emissivity spectra at various temperatures.

(denoted S_0 in Fig. 6), we consider only one-electron excitation from the last occupied subshell. At the second level (S_0+S_1) , we consider also excitation of a second electron from the last occupied subshell. At the third level $(S_0+S_1+S_2)$, excitation of one electron from the second last occupied subshell is added. For the highest level of completeness $(S_0+S_1+S_2+S_3)$ we add excitation of one electron from the second last occupied subshell in S_0 .

The formal definition of the CA rates, i.e. rates connecting fine structure levels within a specific configuration, might make us think that a preliminary calculation of these rates is necessary. This is not the case: following the methods discussed in [16], one can directly calculate CA rates or cross sections for the various relevant processes listed above. The difference

between the various completeness levels can be seen in Fig. 6 with other calculations for comparison. The most sophisticated level is closest to the experimental values in the range 2-3 keV, which gives us confidence that it is the most realistic configuration set.

Another result of our model is the emissivity spectrum over a broad soft-X ray and VUV range. The bremsstrahlung contribution to the emission coefficient is obtained via the classical formula (Kramers) with a correcting free-free Gaunt factor [18]. The radiative recombination (RR) cross sections can be deduced from the inverse process, photoionization, which is evaluated in our CA framework. For bound-bound transitions between two significantly degenerated configurations (i.e. containing a significant number of levels), the resulting profile

is rather *statistical* and reflects the statistical distribution in energy of all the lines connecting the two configurations. This is the strict definition of an Unresolved Transition Array (UTA), i.e., the set of all lines

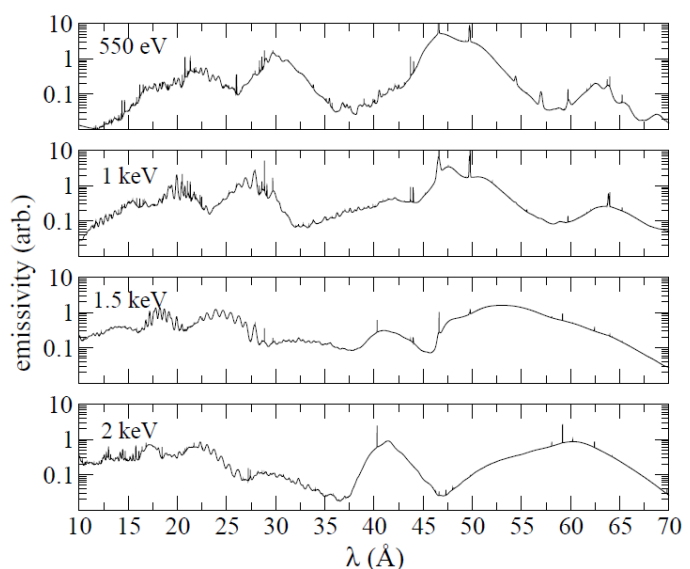


Figure 8: Modelled spectrum in the EUV range for electron temperatures between 0.55 and 2 keV, with the 45-65 Å quasicontinuum clearly visible. The emissivity normalisation is the same for all spectra.

between two configurations. Such a distribution of lines can be characterized by its two first moments (average position and variance).

To avoid a direct line-by-line computation of these moments (which is impractical for a huge number of transitions), one makes use of compact formulas based on operator techniques [19].

It is important to note that a typical relativistic effect such as the spin-orbit interaction may split a single UTA into 2-3 peaks called SOSAs (for spin-orbit split-arrays). A proper implementation of this effect involves a criterion based on the strength of the splitting and on the width of each SOSA.

Among the noticeable defaults of this UTA/SOSA description, one notices a non-inclusion of non-dipole transitions and also a non-inclusion of configuration interaction effects (between different configurations of same parity) which may

affect transition energies and oscillator strengths (particularly for $\Delta n=0$, with n=4 transitions). Another difficulty arises between weakly degenerated pairs of configurations where the number of lines is small and thus the statistical description meaningless.

The results are shown in Fig. 7 for electron temperatures ranging from 1 to 15 keV. It can be seen that, except at low photon energy ad high temperature (e.g. below $h\nu \sim 100$ eV or equivalently above $\lambda \sim 120$ Å at 10 and 15 keV) where free-bound emission dominates, the spectrum is mostly formed of broad spectral features, the so-called quasi-continua, with various shapes and widths.

A calculated spectrum restricted to the short wavelength end of most EUV spectrometers is shown on **Fig. 8**. The strongest feature observed in many tokamaks, namely the quasicontinuum at 45-65 Å, is also found to be the strongest in our calculations. Its structure resembles quite satisfactorily the observed one, with a sharp edge on the left hand side (around 45 Å) of the main feature, a longer wing on the right hand side (50-55 Å) and a secondary feature above 60 Å. This similarities between calculations and observations encourage us to investigate the model predictions in more detail to determine the contributions of individual ionisation stages and possibly their emissivity rate coefficients.

5. ARTIFICIAL INTELLIGENCE ANALYSIS

The 45-65 Å quasicontinuum modelled in the previous section is observed in many tokamaks. Both the model and the observations show that its shape depends on the electron temperature. This is due in particular to the many ionisation stages which contribute differently from each other in this spectral interval. Therefore, we investigated the possibility of deducing the electron temperature from the normalised measured spectra [20]. We use a series of LH-heated discharges (WEST#59845-59852) all performed with the same scenario during a single experimental session. We take advantage of the scanning mode of the spectrometer to work over a wide range of electron temperature.

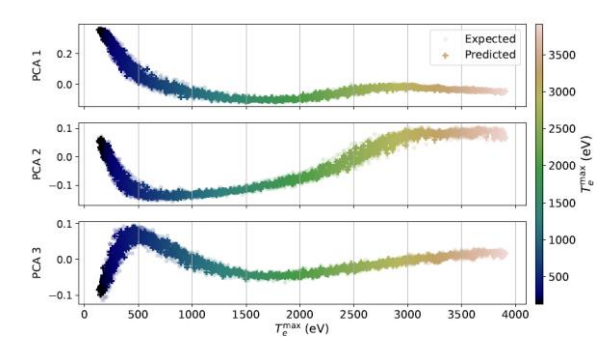


Figure 9: First three components of the PCA as a function of the measured ('expected') maximum temperature along the line of sight.

First, a principal component analysis (PCA) (Fig. 9) has evidenced the correlation between the spectrum shape and the temperature as measured by the WEST ECE diagnostic. It can be seen that the slope of the first two

components is almost flat at the higher end of the temperature range. This may be because the contributing ions $(W^{24+}-W^{35+})$ are abundant [11] mostly in the middle and low temperature range explored here.

We then used a Random Forest (RF) algorithm to study in more detail the temperature predictability. We train the algorithm with measurements from six out of seven discharges with an accuracy better than 150 eV over a broad temperature range (0.5–3.5 keV, see in particular Fig. 4 in [20]). The RF model then successfully generalizes to the seventh shot with comparable accuracy. Such performance can be explained by the strong correlation between the two quantities.

Incidentally, we noticed that for many spectra the model either overestimate or underestimate the temperature, especially in the middle of the investigated temperature range. This is attributed to a possible hysteresis in the mechanical motion of the spectrometer during the measurements. An offline correction to the angle has been introduced. We are now checking that the correction allows to reduce the spread around the diagonal and thus improve our temperature prediction capability.

The reciprocal operation, i.e. spectrum predictions from temperature values, has also been investigated. Given the strong correlation mentioned above, we can reduce the dimensionality of the problem to solely predict the PCA components and reconstruct the full spectra using the PCA inverse transformation. Examples of such predictions are shown in **Figure 10** using either the first two or the first three components of the PCA. It can be seen that the predictions are very close to the measurements with a few exceptions. In particular, a few relatively well resolved spectral lines measured around 48-49 Å at 0.8 keV are not accurately reproduced in the AI predictions. This may suggest that an additional input feature could help capture more spectral lines...

The next step is to investigate the use of the RF algorithm to determine the electron temperature profile along a line of sight of the spectrometer with the same uncertainty. Preliminary tests show that it seems possible. Although not surprising, the reason why reasonable predictions are made without any input about the electron density along the line of sight is puzzling. Indeed, the spectral shape is locally determined by the electron temperature, but the relative contribution of each radial interval depends on the electron density. The final step in this study will be to investigate whether the spectrum at a single temperature can be built with the AI algorithm, in connection with the model described in the previous Section.

6. SUMMARY AND CONCLUSIONS

Spectroscopy measurements in the extreme-UV range are performed in every WEST discharge. As examples of the wealth of information which can be retrieved, we have reported here our investigations on two particular wavelength intervals. In the range 125-135 Å, well identified spectral lines of W^{42+} - W^{44+} are used to determine the Wdensity at temperatures around 2.5-3.5 keV in a highly radiating scenario called X-point radiation (XPR). The W density values deduced from EUV spectroscopy are shown to be comparable with those deduced from bolometry measurements and indicate that the transition to the XPR regime does not have a measurable effect on the W density.

In the second range, 45-65 Å, we attempt to model the strong W quasi-continuum with a type of model adapted from laser-produced plasmas. As a first test of its validity, we show that the average ion charge is consistent with experimental results. Modelling of the spectral emissivity over a broad wavelength range shows that quasicontinuum structures contribute over the whole VUV and soft-X ray range. The 45-65 Å is particularly well modelled when compared to WEST measurements. Investigations will continue

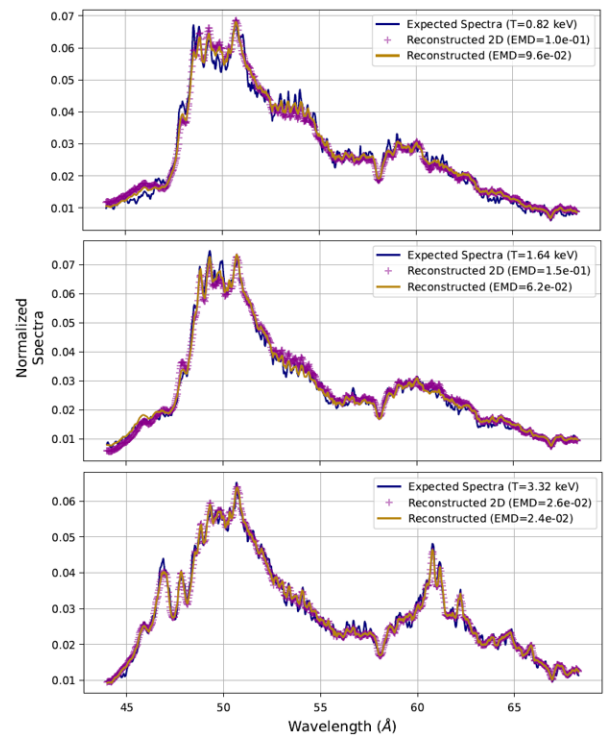


Figure 10: Measured and predicted spectra at various temperatures. +: prediction using the first two components of the PCA, solid line: prediction using the first three components.

about the contributing ions and more broadly, about the possibility to use the model for plasma diagnosis. Finally, this quasi-continuum is used for a tentative temperature diagnostic. A fairly simple Random Forest algorithm is trained on the measurements and used to predict the temperature with uncertainties rarely exceeding

150 eV. A preliminary investigation of the reciprocal prediction (spectrum from temperature) shows encouraging results. Nevertheless, it is not easy to understand if the AI predictions can be related to physics processes and relations. In particular, it seems that predictions can be obtained even without taking into account the electron density profile, despite the fact that it determines the relative contribution of every temperature along the spectrometer line of sight. In the near future, we will investigate the role of both the electron density and temperature with the double aim of predicting the local temperature and of providing experimental spectra at any given temperature as inputs to the atomic physics models such as the one we describe briefly here.

ACKNOWLEDGEMENTS

This work has been carried out within the framework of the EUROfusion Consortium, funded by the European Union via the Euratom Research and Training Programme (Grant Agreement No 101052200 — EUROfusion). Views and opinions expressed are however those of the author(s) only and do not necessarily reflect those of the European Union or the European Commission. Neither the European Union nor the European Commission can be held responsible for them..

Part of this work is supported by the U.S. DOE-OFES under Contract No. DE-AC02-09CH11466.

REFERENCES

- [1] ZOHM, H. et al., Overview of ASDEX-Upgrade results in view of ITER and DEMO, Nucl. Fusion 64 (2024) 112001, DOI: 10.1088/1741-4326/ad249d.
- [2] MAILLOUX, J. et al., Overview of JET results for optimising ITER operation, Nucl. Fusion 62 (2022) 042026, DOI 10.1088/1741-4326/ac47b4.
- [3] MAGET, P. et al., Tungsten control in long pulse operation: feedback from WET to ITER, Plasma Phys. Control. Fusion 67 (2025) 045005, DOI 10.1088/1361-6587/adba0d.
- [4] DESGRANGES, C. et al., submitted to Plasma Phys. Control. Fusion.
- [5] GUIRLET, R. et al., ., Extreme UV spectroscopy measurements and analysis for tungsten density studies in the WEST tokamak, Plasma Phys. Control. Fusion 64 (2022) 105024, DOI: 10.1088/1361-6587/ac8d2c.
- [6] SERTOLI, M. et al, Modification of impurity transport in the presence of saturated (m,n) = (1,1) MHD activity at ASDEX Upgrade, Plasma Phys. Controlled Fusion 57 (2015) 075004.
- [7] GOETZ, J.A., et al., High confinement dissipative divertor operation on Alcator C-mod, Phys. Plasmas 6 (1999) 1899.
- [8] NAKANO, T. et al., Radiation process of carbon ions in JT-60U detched divertor plasmas, J. Nucl. Mater. 390-391 (2009) 255.
- [9] BERNERT, M., et al., X-point radiation, its control and an ELM suppressed radiating regime at the ASDEX Upgrade tokamak, Nucl. Fusion 61 (2021) 024001.
- [10] FAUGERAS, B. et al., An overview of the numerical methods for tokamak plasma equilibrium computation implemented in the NICE code, Fusion Eng. Design 160 (2020) 112020.
- [11] PUETTERICH, T. et al., Modelling of measured tungsten spectra from ASDEX Upgrade and predictions for ITER, Plasma Phys. Control. Fusion 50 (2008) 085016.
- [12] Atomic Data and Analysis Structure (ADAS) (available at: www.adas.ac.uk/)
- [13] BARBUI, T. et al.,
- [14] CHUNG, H.K. et al., FLYCHK: Generalized population kinetics and spectral model for rapid spectroscopic analysis for all elements, High Energy Density Phys. 1 (2005) 3.
- [15] O. CHELLAI et al., 47th EPS Conference on Plasma Physics (2021) P4.1013.
- [16] PEYRUSSE, O., Atomic configuration averages and non-local thermodynamical equilibrium plasma spectroscopy calculations, . Phys. B: At. Mol. Opt. Phys. 32 (1999) 683.
- [17] BAUCHE, J. et al., Role of dielectronic recombination and auto-ionisation states in the dynamic equilibirum of non-LTE plasmas, High Energy Density Phys. 5 (2009) 51.
- [18] KARZAS, W.J. and LATTER, R., Astrophys. J. Suppl. Ser. 6 (1961) 167.
- [19] BAUCHE, J., BAUCHE-ARNOULT, C. and PEYRUSSE, O., Atomic properties in hot plasmas, 2015, Springer.

R. GUIRLET et al.

[Left hand page running head is author's name in Times New Roman 8 point bold capitals, centred. For more than two authors, write **AUTHOR et al.**]

[20] SAURA, N. et al., Machine learning-based tungsten spectroscopy analysis in the WEST tokamak, Phys. Plasmas 32 (2025) 083901.